Computation of Laminar Mixed Convection Flow in a Channel with Wing Type Built-in Obstacles

G. Biswas,* N. K. Mitra,† and M. Fiebig‡
Ruhr Universität Bochum, Bochum, Federal Republic of Germany

The object of this investigation is to compute laminar mixed convection flows and heat transfer in a rectangular channel with a delta wing mounted on the bottom wall. The geometrical configuration represents the proposed model of part of a gas-liquid, fin-pipe crossflow heat exchanger (gas side). Enhancement of heat transfer between the gas and the channel wall is evidenced. This augmentation is primarily due to the longitudinal vortices generated by the wing. Mixed convection condition is characterized by buoyancy induced secondary flows which increase the vortex strength and improve the heat transfer still further.

Nomenclature

B = channel width
b = wing span
c_p = specific heat of the fluid
D = divergence of velocity vectors, Eq. (1)
Gr = Grashof number, $g\beta(T_w - T_\infty)H^3/\nu^2$
g = gravitational acceleration
H = channel height
h = heat transfer coefficient, $-k(\partial T/\partial y)_w/(T_w - T_b)$
k = thermal conductivity of the fluid
Nu = local Nusselt number based on bulk temperature of the fluid, hH/k
Nu_{xe} = local Nusselt number based on entry temperature of the fluid
$\overline{Nu}$ = spanwise average Nusselt number, Eq. (14)
n = iterations in time step
P = nondimensional pressure, $p/\rho U_{av}^2$
p = pressure
Pr = Prandtl number, $\mu c_p/k$
q = wall heat flux
Re = Reynolds number, $U_{av}H/\nu$
S = wing area
T = temperature
t = time
U = u/U_{av}
u = axial component of velocity
V = v/U_{av}
v = vertical component of velocity
W = w/U_{av}
w = spanwise component of velocity
X = x/H
x = axial dimension of coordinates
Y = y/H
y = vertical or normal dimension of coordinates
Z = z/H
z = spanwise dimension of coordinates
α = aspect ratio of the channel, B/H
β = thermal expansion coefficients
ν = kinematic viscosity of the fluid
τ = nondimensional time
Λ = aspect ratio of the wing, b^2/S

Subscripts

w = wall
b = bulk condition
av = average
$s1$ = bottom fin-plate
$s2$ = top fin-plate
sa = spanwise combination of top and bottom plate

Introduction

In gas-liquid, fin-pipe crossflow heat exchangers, fin heat transfer coefficient (gas side) is generally low as compared to that of the pipe (liquid side). Heat transfer from the fins can be enhanced by mounting small protrusions on the fin surfaces. These protrusions also act as spacers for the fins. Protrusions in the form of wings (delta shape) at angle of attack act as strong vortex generators which cause a spiraling flow, hence increasing heat transfer coefficient.[1-3] The longitudinal vortices, formed behind the wing, take fluid from the underside of the wake and swirl it around to upperside, entraining fluid from the outside into the core of the vortices. The use of such kind of wing-generators, therefore, can bring about better mixing of fluid and improve heat transfer in compact gas-liquid, fin-pipe crossflow heat exchangers. Typically, the Reynolds and Mach numbers for such applications lie below 2000 and 0.01, respectively.

If the fluid is treated as incompressible with constant properties (because of a very small characteristic Mach number), the flowfield is decoupled from the temperature field. Computational results of such kind of shear flows with longitudinal vortices have been presented elsewhere.[4] When the flow velocity is not very high and the temperature difference between the body surface and ambient fluid is large, flow and heat transfer characteristics are strongly influenced by thermal buoyancy forces. Even without a vortex generator, buoyancy can induce longitudinal vortices and multiple plumes which can enhance heat transfer and alter the length of the entrance region in mixed convection flows in ducts.[5,6] Because the flow structure observed in mixed convection horizontal flow is quite complex, there is a general agreement that more research on the subject is required.

Arising out of the practical and academic importance of the flow configuration and thermal conditions as enumerated above, a need is felt to compute three-dimensional laminar mixed convection flow in a horizontal channel with built-in

Received May 6, 1988; presented as Paper 88-2647 at the AIAA Thermophysics, Plasmadynamics, and Lasers Conference, San Antonio, TX, June 27-29, 1988; revision received Oct. 7, 1988.

*Alexander von Humboldt Fellow from Indian Institute of Technology, Kharagpur, India.
†Scientist, Institut für Thermo- und Fluiddynamik. Member AIAA.
‡Professor of Heat and Mass Transfer, Institut für Thermo- und Fluiddynamik.

wing type obstacles. For detailed investigations, only one vortex generator inside a horizontal channel has been considered. In practice, the wings can easily be manufactured by punching or embossing the channel wall. However, the effects due to the hole beneath the wing-generator have not been taken into account in this model. To include the effect of thermal buoyancy, Boussinesq approximation has been used and the flow medium has been treated as incompressible.

Statement of the Problem

Computation is performed in a channel which is formed by two neighboring fins (Fig. 1a). An obstacle in the form of a delta wing (of zero thickness) is placed inside it. The base of the wing is fixed on the bottom plate and the apex faces the incoming flowstream with an angle of attack. The buoyancy-driven flow interacts with the laminar main flow to yield mixed convection conditions. Since symmetry prevails in the vertical central plane of the channel, flowfield only in half of the channel has to be computed. The dimensionless equations for continuity, momentum, and energy with the Boussinesq approximation may be expressed in the following conservative form as

$$D = \frac{\partial U}{\partial X} + \frac{\partial V}{\partial Y} + \frac{\partial W}{\partial Z} = 0 \tag{1}$$

$$\frac{\partial U}{\partial \tau} + \frac{\partial U^2}{\partial X} + \frac{\partial UV}{\partial Y} + \frac{\partial UW}{\partial Z} = -\frac{\partial P}{\partial X} + \frac{\nabla^2 U}{Re} \tag{2}$$

$$\frac{\partial V}{\partial \tau} + \frac{\partial UV}{\partial X} + \frac{\partial V^2}{\partial Y} + \frac{\partial VW}{\partial Z} = -\frac{\partial P}{\partial Y} + \frac{\nabla^2 V}{Re} + \frac{Gr}{Re^2}\theta \tag{3}$$

$$\frac{\partial W}{\partial \tau} + \frac{\partial UW}{\partial X} + \frac{\partial VW}{\partial Y} + \frac{\partial W^2}{\partial Z} = -\frac{\partial P}{\partial Z} + \frac{\nabla^2 W}{Re} \tag{4}$$

$$\frac{\partial \theta}{\partial \tau} + \frac{\partial U\theta}{\partial X} + \frac{\partial V\theta}{\partial Y} + \frac{\partial W\theta}{\partial Z} = \frac{\nabla^2 \theta}{Re \cdot Pr} \tag{5}$$

In the above equations, the velocity has been nondimensionalized with the average incoming velocity U_{av} at the channel inlet; all lengths have been nondimensionalized with the channel height H; and the pressure with ρU_{av}^2 and the nondimensional temperature is defined as $\theta = (T - T_\infty)/(T_w - T_\infty)$. Boundary conditions of interest in this investigation are for top and bottom surfaces

$$u = v = w = 0; \qquad T = T_w$$

for sidewall ($z = B/2$) and midplane ($z = 0$)

$$w = (\partial v/\partial z) = (\partial u/\partial z) = (\partial T/\partial z) = 0$$

At the channel inlet, normal and spanwise components of velocity are assumed to be zero, and a fully-developed profile for the axial velocity is deployed. The temperature of the incoming stream T_∞ is assumed to be constant. At the exit, the boundary conditions for the dependent variables are obtained by setting their second derivatives in the x direction equal to zero in order to ensure a smooth transition through the outflow boundary. No-slip boundary conditions for the velocities on the obstacle are used. The temperature of the obstacle is constant and equal to T_w. In order to state further details about the kinematic conditions on the wing, specific examples can be discussed with the help of Fig. 1b. The axial and the vertical components of velocity that fall directly on the wing are set to zero. Spanwise components do not fall directly on the wing. These w velocities are interpolated on the wing from neighboring cells and then the interpolated velocity components are set equal to zero.

Method of Solution

A modified version of the Marker and Cell (MAC) method[7,8] is used to obtain the numerical solution of Eqs. (1–5). The computational domain is divided into a set of Cartesian cells (Fig. 2a). Staggered grid arrangements are used in which velocity components are defined at the cell faces to which they are normal (Fig. 2b). The pressure and temperature are defined at the center of the cell.

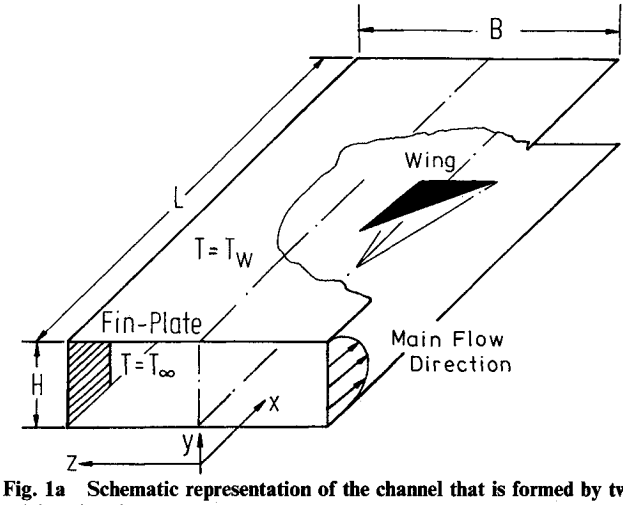

Fig. 1a Schematic representation of the channel that is formed by two neighboring fins.

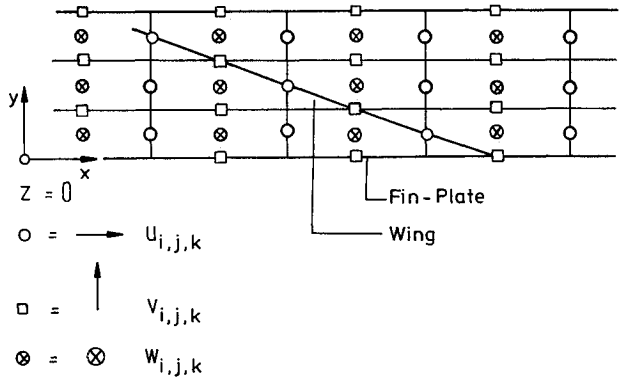

Fig. 1b Relative locations of the fin-plate, wing, and velocity components (front elevation about the midplane of the channel).

The computation of velocity and temperature fields are coupled. To start a computational cycle, guessed fields for velocity, pressure, and temperature are used. From these fields, corrected pressure and velocity fields are obtained by pressure and velocity iterations through a continuity equation, discussion of which will follow. From the initial temperature field and the aforesaid corrected velocity field, temperature distribution for the first cycle is calculated from the energy equation. This new temperature field and the foregoing corrected velocity and pressure fields are used to calculate Navier-Stokes Eqs. (2–4) to evaluate velocities for the next time increment. As such, in the subsequent cycles solutions for velocities are obtained in two folds. First, the velocity components are advanced explicitly using the previous state of flow to calculate accelerations caused by convections, viscous stresses, pressure gradients, and buoyancy interactions through a time step of duration $\delta\tau$. The explicit time increment may not necessarily lead to a velocity field with a zero mass divergence in each cell. In the subsequent second fold, adjustment of pressure and velocity is done by an iterative process in order to ensure mass conservation in each cell. This iterative correction of velocity field through implicit continuity equation is equivalent to solution of a Poisson equation for pressure.[9] The convective terms of the Eqs. (2–4) are discretized by a weighted average of upwind and central differences. Here, the formal first-order accuracy $O(\Delta X)$ of the upwind differencing scheme retains 'something' of the second-order accuracy of the advection field.[10] In calculations

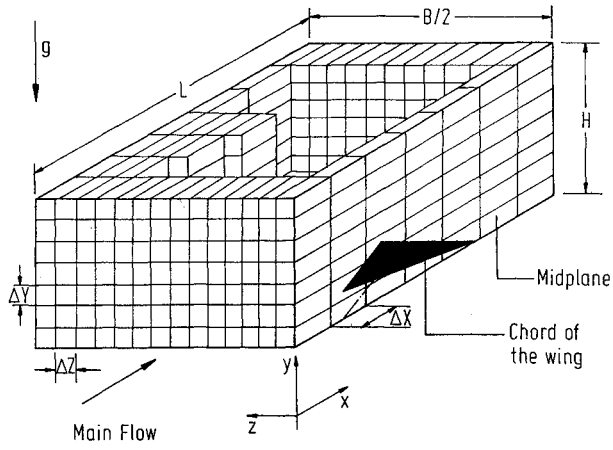

Fig. 2a Grid spacing in the computational domain and the location of the wing generator.

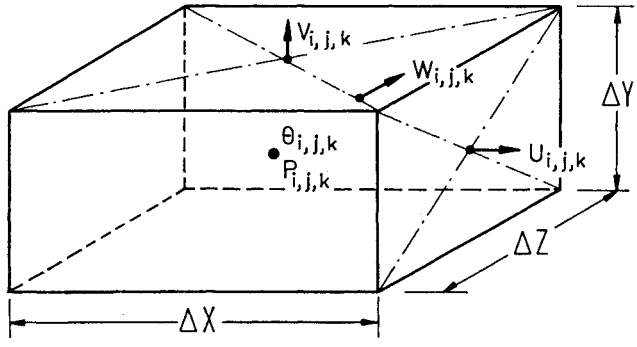

Fig. 2b Three-dimensional staggered grid showing the locations of the discretized variables.

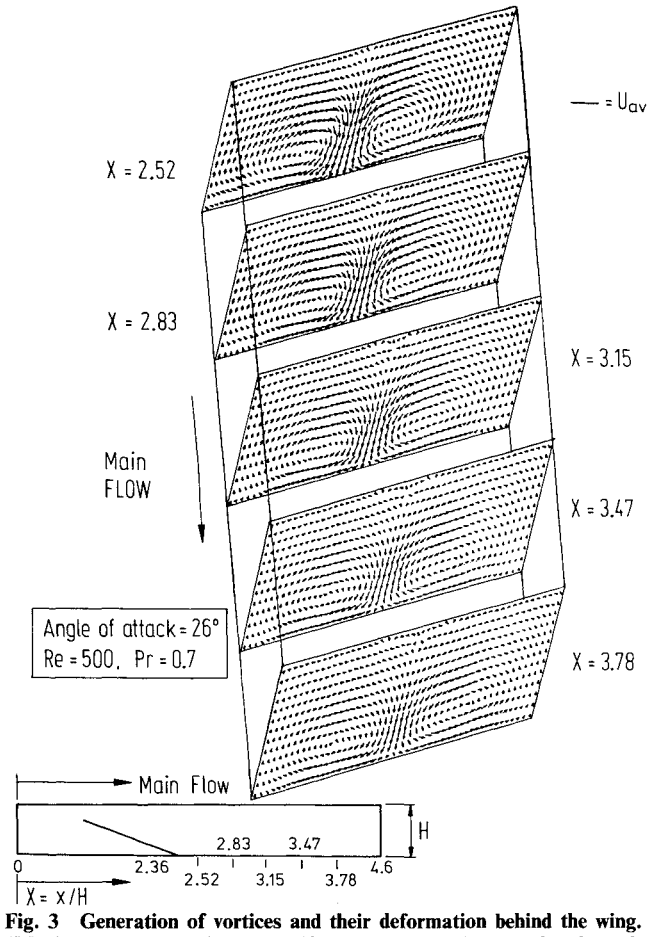

Fig. 3 Generation of vortices and their deformation behind the wing. Velocity vectors are shown at different cross sections in the channel. Aspect ratio of the channel $\alpha = 2$ and the aspect ratio of the wing $\Lambda = 1$. The base of the wing is located at a distance $X = 2.36$ from the inlet.

of driven cavity flows, Torrance et al.[11] showed that the second upwind method applied to the conservative form of equations is indeed superior to the second-order differencing applied to the nonconservative form of equations.

A concise description of mathematical methodology for pressure-velocity iteration is described herein. In each cell (i, j, k), the value of the velocity divergence D is calculated from Eq. (1). If the magnitude of D is larger than a prescribed small value ε, the pressure in each cell is adjusted proportionally to negative of velocity divergence by

$$\delta p^n_{i,j,k} = -\omega D^n_{i,j,k} \tag{6}$$

where ω is defined as

$$\omega = \omega_o \Big/ \left[2\delta\tau \left(\frac{1}{\delta X^2} + \frac{1}{\delta Y^2} + \frac{1}{\delta Z^2} \right) \right] \tag{7}$$

The factor ω_o is an overrelaxation factor. After $\delta P_{i,j,k}$ has been calculated for a cell, it is necessary to add it to cell pressure $P_{i,j,k}$ and to adjust the velocity components on the sides of cell (i,j,k) according to

$$U^{n+1}_{i,j,k} \to U^{n+1}_{i,j,k} + (\delta\tau \cdot \delta P^n_{i,j,k})/\delta X \tag{8}$$

$$U^{n+1}_{i-1,j,k} \to U^{n+1}_{i-1,j,k} - (\delta\tau \cdot \delta P^n_{i,j,k})/\delta X \tag{9}$$

$$V^{n+1}_{i,j,k} \to V^{n+1}_{i,j,k} + (\delta\tau \cdot \delta P^n_{i,j,k})/\delta Y \tag{10}$$

$$V^{n+1}_{i,j-1,k} \to V^{n+1}_{i,j-1,k} - (\delta\tau \cdot \delta P^n_{i,j,k})/\delta Y \tag{11}$$

$$W^{n+1}_{i,j,k} \to W^{n+1}_{i,j,k} + (\delta\tau \cdot \delta P^n_{i,j,k})/\delta Z \tag{12}$$

$$W^{n+1}_{i,j,k-1} \to W^{n+1}_{i,j,k-1} - (\delta\tau \cdot \delta P^n_{i,j,k})/\delta Z \tag{13}$$

This process is repeated successively in all cells until no cell has a magnitude of D greater than ε. After evaluating correct velocities, the energy equation is solved with a successive over-relaxation (SOR) technique to determine the temperature field. This scheme of solution is continued until a steady flow is obtained. The procedure avoids the need of pressure boundary conditions, as associated with the solution for the Poisson equation for pressure.[12] The computations have been performed on a Prime 2250 computer. The computational domain is divided into 36 grid nodes in the x direction. A 15×26 cross stream grid is employed in the y-z plane.

Computational accuracy is calibrated by comparing the peripheral average local Nusselt numbers predicted by our numerical scheme with those of available literature[16] for thermally developing and hydrodynamically developed flow through parallel plates. The results are found to be in agreement within about 5% for forced flow with Reynolds number of 500 and uniform wall temperature boundary condition.

For the forced convection flow ($Re = 500$, $Pr = 0.7$) in a channel with built-in delta wing, grid development behavior is discerned by observing reasonable agreement between the results obtained for 15×26 and 20×30 cross-stream grids. However, grid, independence studies could not be conducted for different Grashof numbers owing to the massive computational time on a Prime machine.

Results and Discussion

A number of computations have been performed with and without free convection at different Re (500, 1815) and Gr and angles of attack (20 and 26). The results typically show the generation of vortices and their elliptic deformation as they move along the channel (Fig. 3).

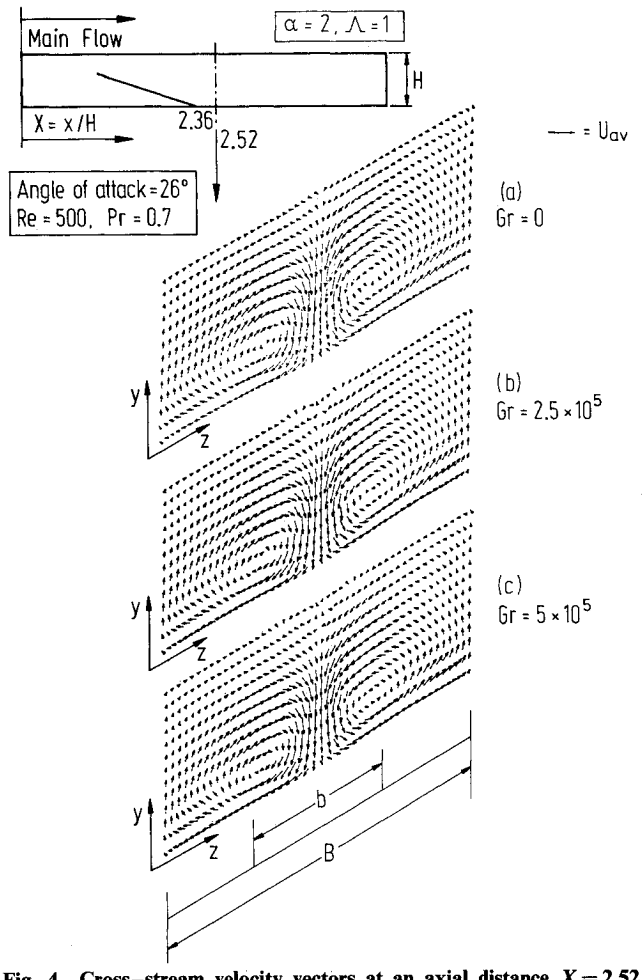

Fig. 4 Cross-stream velocity vectors at an axial distance $X = 2.52$ from the inlet of the channel for different Grashof numbers.

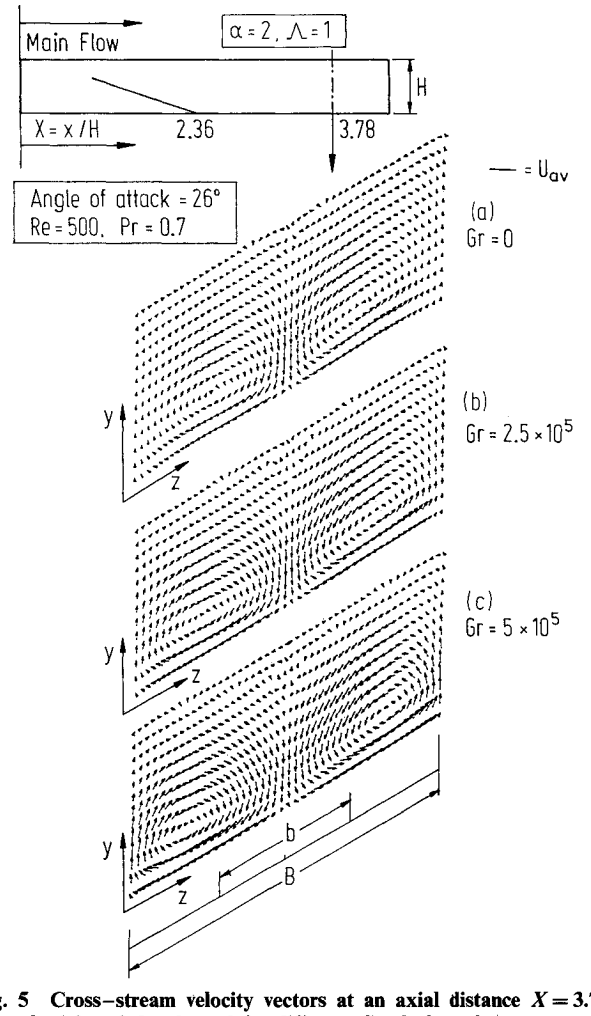

Fig. 5 Cross-stream velocity vectors at an axial distance $X = 3.78$ from the inlet of the channel for different Grashof numbers.

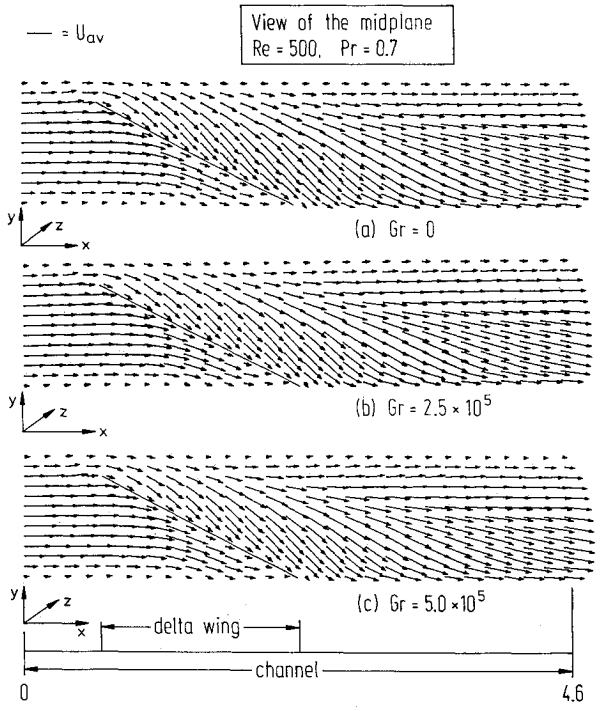

Fig. 6 Velocity vectors on a longitudinal section (x-y plane) of the channel. The views are taken about the midplane for $\alpha = 2$ and $\Lambda = 1$.

Figures 4a–4c compare the cross-stream velocity vectors for $Re = 500$ at a nondimensional distance $X = 2.52$ from the inlet of the channel for the cases without ($Gr = 0$) and with free convection ($Gr = 2.5 \times 10^5$, $Gr = 5.0 \times 10^5$), respectively. The axial location of this crossplane is situated in the immediate neighborhood behind the wing base. Here, the strength of the secondary vortices, due to the wing, is so high that free convection does not bring any noticeable change. But a somewhat different trend is observed from the plots of cross-stream vectors farther downstream at $X = 3.78$ (Figs. 5a–5c). Here the strength of the vortex pair due to the wing is reduced owing to the viscous resistance experienced by the vortices in the course of their travel along the channel (Fig. 5a). When the influence of thermal buoyancy is superimposed, counter-rotating vortices with higher strength preeminently reappear in the same axial location (Figs. 5b and 5c). A closer observation illustrates that the vortex strength is increased with increasing Grashof number. Centers of the vortices also shift more toward the side walls when the magnitude of thermal buoyancy is larger.

Velocity vectors on the longitudinal section (x-y plane) for different values of a Grashof number and a fixed Reynolds number are shown in Figs. 6a–6c. The views are taken about the midplane of the channel. Spiralling flow structure is discerned behind the wing for all the cases. The influence of thermal buoyancy is not well-pronounced on this longitudinal section. But at a nondimensional distance $Z = 0.38$ away from the midplane, a different trend could be witnessed from the velocity vector plots on the longitudinal section for different values of Grashof numbers (Figs. 7a–7c). Downstream, the location of the maximum value of the axial velocity profile shifts towards the bottom wall, more so in the case of larger Grashof number. This Grashof number dependence of axial velocity profiles resembles the findings of theoretical studies of Cheng and Hwang[13] and Hishida, Nagano, and Montes-

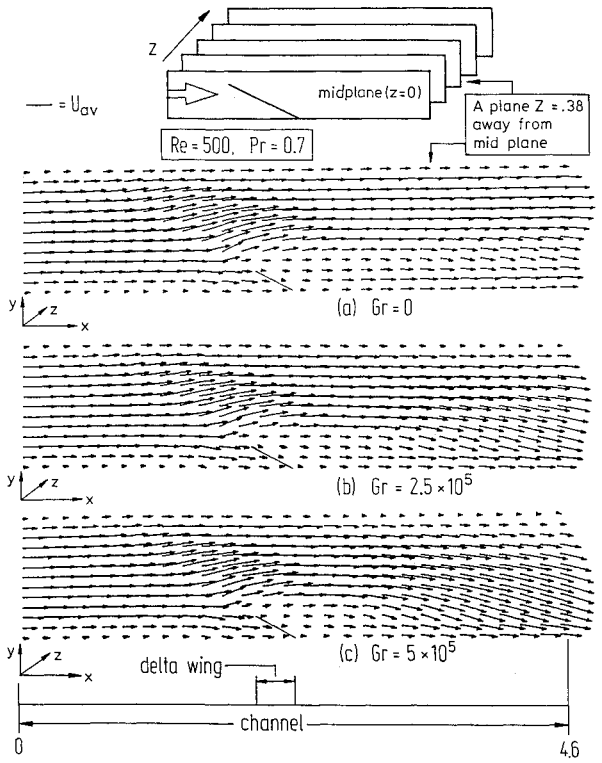

Fig. 7 Velocity vectors on a longitudinal section (x-y plane) at a distance $Z = 0.38$ away from the midplane for $\alpha = 2$ and $\Lambda = 1$.

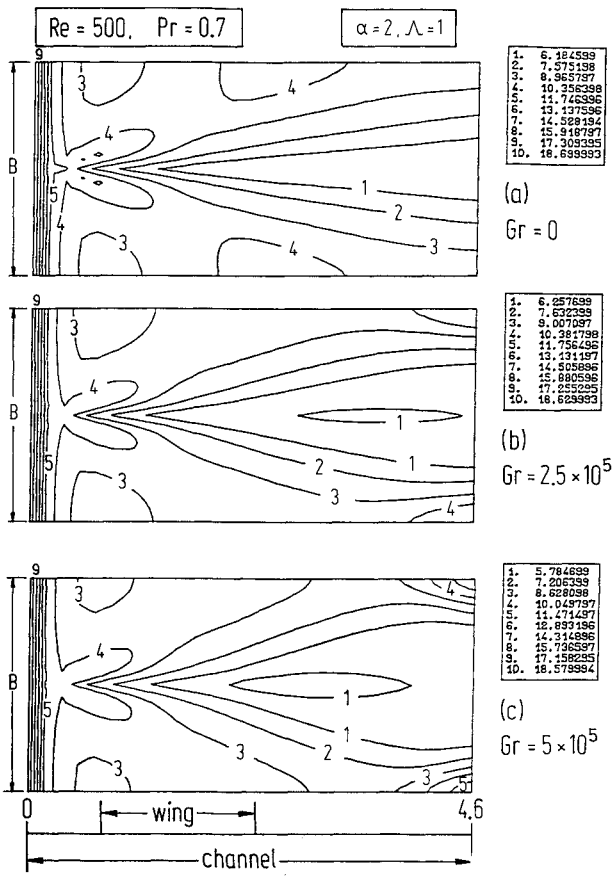

Fig. 8 Iso-lines for Nusselt number on the top fin-plate.

claros.[14] In another study, Newell and Bergles[15] also observed this influence of the Grashof number on axial velocity profiles.

Figures 8a–8c show the equivalent Nusselt number distribution on the top plate of the channel for three different Grashof numbers and for $Re = 500$. The zone of the lower

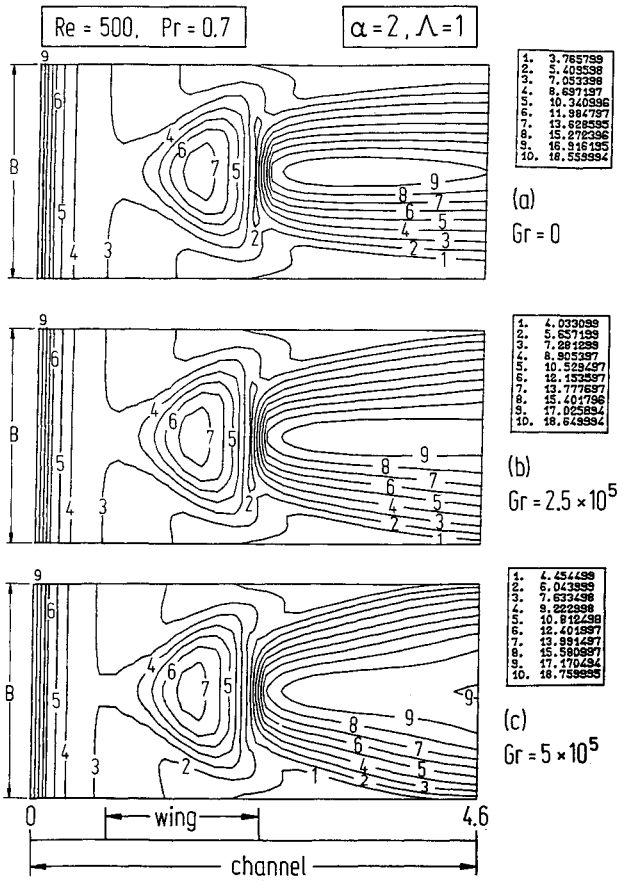

Fig. 9 Iso-lines for Nusselt number on the bottom fin-plate.

Nusselt number increases downstream with an increasing Grashof number. This signifies deterioration of heat transfer on the upper plate of the channel, with increasing upward thermal buoyancy.

Figures 9a–9c show the isolines for Nusselt numbers on the bottom plate of the channel. With an increasing Grashof number, the zone of the higher Nusselt number increases behind the wing. It can be said that heat transfer on the bottom plate is enhanced by buoyancy driven secondary flow.

In order to have a better understanding of the heat transfer performance, the spanwise average Nusselt number

$$\overline{Nu} = \frac{Bq}{2\int_0^{B/2} [T_w(x, z) - T_b(x)]\, dz} \cdot \frac{H}{k} \qquad (14)$$

has been calculated at each longitudinal location on both the top and the bottom wall, and the distributions are plotted. Figure 10 shows the effect of the Grashof number on longitudinal distribution of the spanwise average Nusselt number on the bottom plate of the channel. For all cases, near the inlet, the spanwise average Nusselt number distributions follow their usual trend of decay from a very high to a low value. In the region of the wing (from $X = 0.78$ to $X = 2.36$), spanwise average Nusselt number in each case rises to a high value up to a region behind the middle of the wing and then descends. A small dead water zone exists near the wing-body junction that eventually causes poor heat transfer in this location. However, farther downstream behind the wing, heat transfer is increased for all the cases, primarily due to the secondary vortices generated by the wing. In this region, thermal buoyancy plays an additional but significant role. Spanwise average Nusselt number value increases with an increasing Grashof number. Strength of the longitudinal vortices behind the wing increases with increasing magnitude of thermal buoyancy, which improves the heat transfer on the bottom plate at large.

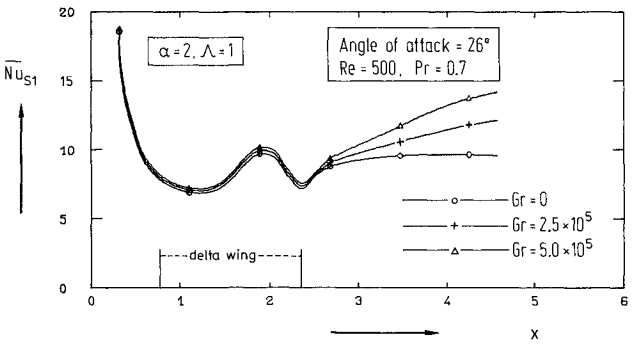

Fig. 10 Effect of the Grashof number on longitudinal distribution of the spanwise average Nusselt number on the bottom fin-plate.

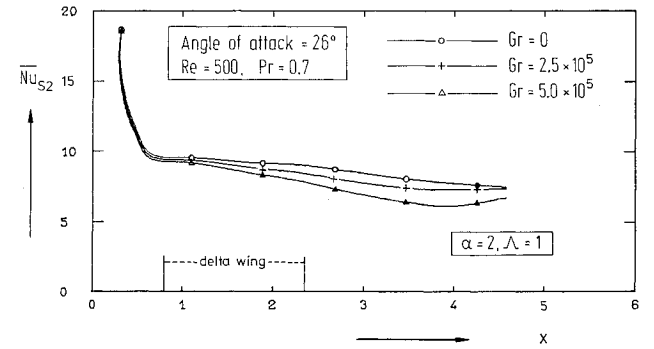

Fig. 11 Effect of the Grashof number on longitudinal distribution of the spanwise average Nusselt number on the top fin-plate.

Longitudinal distribution of spanwise average Nusselt number on the top channel wall is shown in Fig. 11. Increasing Grashof number results in a decrease in spanwise average Nusselt number on the top plate. Upward drift of hot fluid causes a reduction in heat transfer on the upper plate.

Heat transfer performance in the channel can be summarized by combining longitudinal distribution of a spanwise average Nusselt number of both the top and the bottom plates. Figure 12 illustrates the combined spanwise average Nusselt number distribution in the channel. Net effect of the Grashof number on heat transfer in the channel is better understood from these plots. Beyond a nondimensional distance $X = 3.154$, the spanwise average Nusselt number increases with an increasing Grashof number. At the channel exit, $\overline{Nu}_{sa}$ for $Gr = 5.0 \times 10^5$ is 22.48% larger than for $Gr = 0$. At this juncture, it is necessary to show the change in combined spanwise average Nusselt number distribution in the channel brought about by the wing without being influenced by free convection. This is clarified by the plot of combined spanwise average Nusselt number distribution in the channel without built-in delta wing. Augmentation of heat transfer is remarkably evidenced even without any influence of thermal buoyancy. The increase of $\overline{Nu}_{sa}$ for the case of forced flow with built-in obstacle above the forced flow without any obstacle (78.45% at the exit of the channel) is due to secondary flow, generated by the wing and the subsequent development of counter-rotating vortices. The vortices mix the cooler fluid from the core with the hot fluid from the plate surface. This disrupts the growth of thermal boundary layer and, thereby, increases heat transfer to a large extent.

Because of nonavailability of an experimental data base for mixed convection flow in a similar kind of geometry, the model validation was performed through comparison with several published experimental results for forced convection. Local Nusselt numbers along the centerline at the bottom plate with a delta wing at an angle of attack 20 deg are calculated. Reynolds and Prandtl numbers for this computation are 1815 and 0.7, respectively. Here, local Nusselt number values were calculated on the basis of the entry

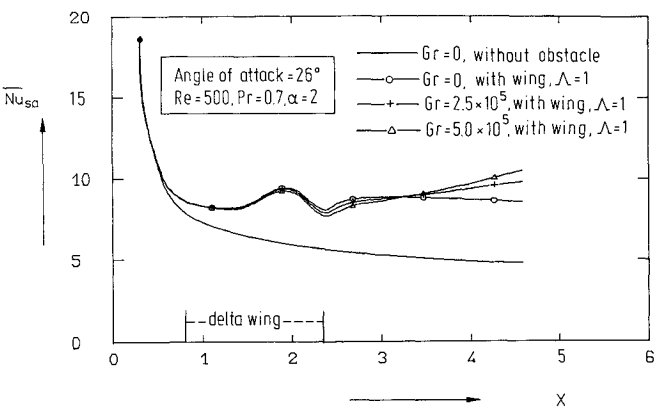

Fig. 12 Effect of the Grashof number and wing on longitudinal distribution of the combined spanwise average Nusselt number in the channel.

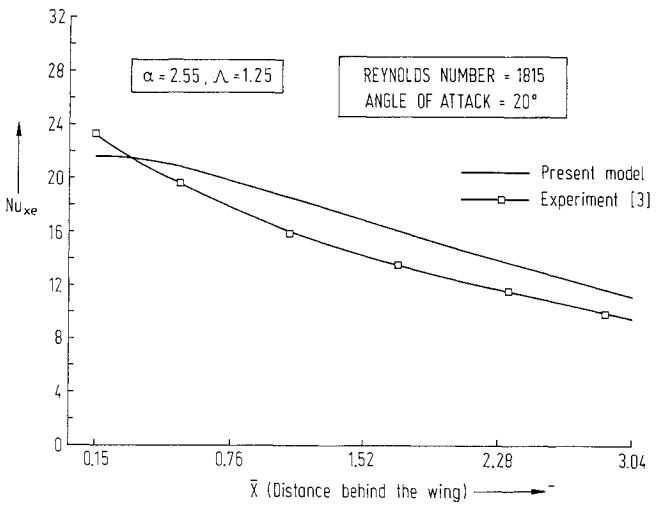

Fig. 13 Local Nusselt number along the centerline for a fin-plate (bottom fin-plate) with a delta wing. Computed values have been compared with experimental results.

temperature of the incoming fluid stream. Figure 13 shows that the computed values of the local Nusselt number compare favorably with the experimental results of Fiebig, Kallweit, and Mitra.[3] The discrepancy is, indeed, not very much pronounced. The difference could be attributed primarily to the flow loss beneath the punched wing-generator in the experiments. The punched hole has not been taken into account in the present computational model. This leads to underprediction of the experimental results. Further, it was not possible to maintain perfect isothermal conditions on the plate surface in the experiments. Since the intensity of turbulence was less than 2% in the experiments,[3,17] its influence on the discrepancy of results can possibly be ignored.

Concluding Remarks

Overall effect of the wing-type vortex generators is to form secondary vortices behind the wing that disrupt the development of themal boundary layer and increase heat transfer. Over and above, the free convection enhances the strength of the counter-rotating vortices behind the wing and, consequently, heat transfer improves still further. In general, the mixed convection condition is characterized by buoyancy-driven secondary flows that form counter-rotating vortices of the same orientation as the delta wing. Assessing the model, in terms of agreement with the experimental observation, it can be rated as fair. Need remains for a critical judgement regarding the excellence of the model. This task can be accomplished through comparison with various other experimental results.

Acknowledgment

G. Biswas gratefully acknowledges the financial support provided by the Alexander von Humboldt Stiftung, Federal Republic of Germany.

References

[1]Edwards, F. J. and Alker, G. J. R., "The Improvement of Forced Convection Surface Heat Transfer Using Surface Protrusions in the Form of (A) Cubes and (B) Vortex Generators," *Proceedings of the Fifth International Heat Transfer Conference*, Vol. 2, Japan Society of Mechanical Engineers, Tokyo, 1974, pp. 2244–2248.

[2]Russel, C. M. B., Jones, T. V., and Lee, G. H., "Heat Transfer Enhancement Using Vortex Generators," *Proceedings of the Seventh International Heat Transfer Conference*, Vol. 3, Hemisphere, New York, 1982, pp. 283–288.

[3]Fiebig, M., Kallweit, P., and Mitra, N. K., "Wing Type Vortex Generators for Heat Transfer Enhancement," *Proceedings of the Eighth International Heat Transfer Conference*, Vol. 6, Hemisphere, New York, 1986, pp. 2909–2913.

[4]Brockmeier, U., Mitra, N. K., and Fiebig, F., "Navier-Stokes Computation of Three-Dimensional Laminar Flowfields in a Channel with a Wing Type Vortex Generator," *Proceedings of the Second International Symposium on Computational Fluid Dynamics*, edited by G. de Val Davis and C. A. J. Fletcher, North-Holland, Amsterdam 1987.

[5]Incropera, F. P. and Schutt, J. A., "Numerical Simulation of Laminar Mixed Convection in the Entrance Region of Horizontal Rectangular Ducts," *Numerical Heat Transfer*, Vol. 8, Nov.–Dec. 1985, pp. 707–729.

[6]Incropera, F. P., Knox, A. L., and Maughan, J. R., "Mixed Convection Flow and Heat Transfer in the Entry Region of a Horizontal Rectangular Duct," *Journal of Heat Transfer*, Vol. 109, May 1987, pp. 434–439.

[7]Harlow, F. H. and Welch, J. E., "Numerical Calculation of Time-Dependent Viscous Incompressible Flow of Fluid with Free Surface," *The Physics of Fluids*, Vol. 8, Dec. 1965, pp. 2182–2188.

[8]Hirt, C. W. and Cook, J. L., "Calculating Three-Dimensional Flows Around Structures and Over Rough Terrain," *Journal of Computational Physics*, Vol. 10, Oct. 1972, pp. 324–340.

[9]Brandt, A., Dendy, J. E., and Ruppel, H., "The Multigrid Method for Semi-Implicit Hydrodynamic Codes," *Journal of Computational Physics*, Vol. 34, March 1980, pp. 348–370.

[10]Roche, P. J., *Computational Fluid Dynamics*, Hermosa, Albuquerque, NM, 1972, pp. 73–74.

[11]Torrance, K., Davis, R., Eike, K., Gill, P., Gutman, D., Hsui, A., Lyons, S., and Zien, H., "Cavity Flows Driven by Buoyancy and Shear," *Journal of Fluid Mechanics*, Vol. 51, Part 2, Jan. 1972, pp. 221–231.

[12]Peyret, R. and Taylor, T. D., *Computational Methods for Fluid Flow*, Springer Series in Computational Physics, Springer-Verlag, New York, 1983, pp. 150–164.

[13]Cheng, K. C. and Hwang, G. J., "Numerical Solution for Combined Free and Forced Laminar Convection in Horizontal Rectangular Channels," *Journal of Heat Transfer*, Vol. 91, Feb. 1969, pp. 59–66.

[14]Hishida, M., Nagano, Y., and Montesclaros, M. S., "Combined Forced and Free Convection in the Entrance Region of a Isothermally Heated Horizontal Pipe," *Journal of Heat Transfer*, Vol. 104, Feb. 1982, pp. 153–159.

[15]Newell, P. H., Jr. and Bergles, A. E., "Analysis of Combined Free and Forced Convection for Fully Developed Laminar Flow in Horizontal Tubes," *Journal of Heat Transfer*, Vol. 91, Feb. 1970, pp. 83–93.

[16]Shah, R. K. and London, A. L., "Laminar Flow Forced Convection in Ducts," *Advances in Heat Transfer*, Suppl. 1, Academic, New York, 1978, pp. 169–176.

[17]Kallweit, P., "Längswirbelerzeuger für den Einsatz im Lamellenwärmetauscher," Doctoral Thesis, Inst. für Thermo- und Fluiddynamik, Ruhr-Universität Bochum, Federal Republic of Germany, 1986, pp. 27–28.